Changes in global teleconnection patterns under global warming and stratospheric aerosol intervention scenarios

**Abolfazl Rezaei[1, 2, *], Khalil Karami[3], Simone Tilmes[4], & John C. Moore[5, 6, 7]**

[1] Department of Earth Sciences, Institute for Advanced Studies in Basic Sciences, Zanjan 45137–66731, Iran. arezaei@iasbs.ac.ir; abolfazlrezaei64@gmail.com.

[2] Center for Research in Climate Change and Global Warming (CRCC), Institute for Advanced Studies in Basic Sciences (IASBS), Zanjan 45137–66731, Iran.

[3] Institut für Meteorologie, Stephanstraße 3, 04103 Leipzig, Germany. khalil.karami@uni-leipzig.de

[4] National Center for Atmospheric Research, Boulder, CO, USA. tilmes@ucar.edu

[5] College of Global Change and Earth System Science, Beijing Normal University, Beijing, 100875, China. john.moore.bnu@gmail.com

[6] CAS Center for Excellence in Tibetan Plateau Earth Sciences, Beijing, 100101, China.

[7] Arctic Centre, University of Lapland, Rovaniemi, 96101, Finland.

* Corresponding Author: Abolfazl Rezaei, Department of Earth Sciences, Institute for Advanced Studies in Basic Sciences, Zanjan 45137–66731, Iran. arezaei@iasbs.ac.ir; abolfazlrezaei64@gmail.com.

**Abstract**

We investigate the potential impact of Stratospheric Aerosol Intervention (SAI) on the spatiotemporal behavior of large-scale climate teleconnection patterns represented by the North Atlantic Oscillation (NAO), Pacific Decadal Oscillation (PDO), El Niño/Southern Oscillation (ENSO) and Atlantic Multidecadal Oscillation (AMO) indices using simulations from the Community Earth System Models (CESM1 and CESM2). The leading Empirical Orthogonal Function of sea surface temperature (SST) anomalies indicates that greenhouse gas (GHG) forcing is accompanied by increases in variance across both the North Atlantic (i.e., AMO) and North Pacific (i.e., PDO) and a decrease over the tropical Pacific (i.e., ENSO); however, SAI effectively reverses these global warming-imposed changes. The projected spatial patterns of SST anomaly related to ENSO show no significant change under either global warming or SAI. In contrast, the spatial anomaly patterns pertaining to AMO (i.e., in the North Atlantic) and PDO (i.e., in the North Pacific) changes under global warming are effectively suppressed by SAI. For AMO, the low contrast between the cold-tongue

pattern and its surroundings in the North Atlantic, predicted under global warming, is restored under SAI scenarios to similar patterns as in the historical period. The frequencies of El Niño and La Niña episodes modestly increase with GHG emissions in CESM2, while SAI tends to compensate for them. All climate indices' dominant modes of inter-annual variability are projected to be preserved in both warming and SAI scenarios. However, the dominant decadal and interdecadal variability mode changes induced by global warming are exacerbated by SAI, particularly in the Atlantic-based AMO. Nonetheless, these findings are limited by the data available, especially for multi-decadal signals, with less than 100-year long simulations available for SAI.

**Keywords:** Ocean-atmosphere teleconnection patterns; GLENS; SSP5-8.5; Stratospheric Aerosol Intervention; Global warming

**500-character non-technical text**

Teleconnection patterns are important characteristics of the climate system, well-known examples include the El Niño and La Niña events driven from the tropical Pacific. We examined how patterns that arise in the Pacific and Atlantic Oceans behave under stratospheric aerosol geoengineering and greenhouse gas (GHG)-induced warming. In general, geoengineering reverses trends, however in the Atlantic, the multidecadal oscillation that is shifted to higher frequencies by GHG is further strengthened.

**1. Introduction**

Although the Paris agreement and accompanying international commitments to decrease carbon emissions are an essential step forward, current nationally contributions have only about a 50% chance to restrict global mean temperature increase to 2°C above preindustrial (Meinshausen et al., 2022). Exceeding 2°C will lead to severe consequences and societal disruption worldwide as humanity is critically dependent on ecosystems, food, fresh water, and health systems which face rapidly challenging adaptation pressure above 2°C of global warming (Field and Barros, 2014).

In parallel with emissions reductions, solar radiation modification (SRM) has been suggested to limit global temperature increases and consequent climate impacts from anthropogenic greenhouse gas (GHG) emissions. A naturally occurring analog of SRM is the well-known global surface cooling following large volcanic eruptions, albeit over relatively short periods. Simulations have shown that SRM decreasing total solar irradiance by about 2%, would roughly compensate for global warming from a doubling of $CO_2$ concentrations (Dagon and Schrag, 2016).

66    Oceans act as major drivers of climate variability worldwide (e.g., Shukla, 1998; Cai et al., 2021), and

67    more than 90% of the excess energy balance of the earth arising from GHG emissions ends up heating

68    the ocean (Cheng et al., 2015). Variations in sea surface temperatures (SSTs) and the global climate

69    are linked through ocean-atmosphere energy exchanges that can be helpfully summarized by climate

70    indices that characterize large-scale climate teleconnection patterns. That is recurring and

71    persistent, large-scale anomaly patterns of pressure and circulation across large geographical

72    regions. Some of the most referred to are El Niño/Southern Oscillation (ENSO), Pacific Decadal

73    Oscillation (PDO), Atlantic Multidecadal Oscillation (AMO), and North Atlantic Oscillation (NAO). The

74    dominant inter-annual feature of climate variability on the planet is ENSO, and its state produces

75    widespread climatic and environmental outcomes (Latif and Keenlyside, 2009). The PDO modulates

76    marine ecosystems and global climate on decadal time scales (Mantua et al., 1997), impacts ENSO

77    onset and frequency (Fang et al., 2014), and is useful for short- to long-term climate forecast (An and

78    Wang, 1999). The AMO has broader hemispheric impacts beyond North American and European

79    climates (Enfield et al. 2001), influencing the monsoons across North African, East Asia, and India

80    (Zhang and Delworth 2006). The NAO is among the dominant climate variability modes in the

81    northern hemisphere (Simpkins, 2021).

82    Several studies have explored how climate indices, particularly ENSO, respond to global warming

83    and increasing GHG concentrations. Statistically significant systemic changes have occurred in ENSO

84    dynamics and the evolution of El Niño and La Niña events since the 1960s (Moron et al., 1998;

85    Capotondi and Sardeshmukh, 2017). ENSO may favor more severe events under global warming

86    (Fedorov and Philander, 2001), and Cai et al. (2015) found that ENSO-associated disastrous weather

87    consequences tend to arise more frequently under unabated $CO_2$ emissions. Cai et al. (2021) found

88    an inter-model consensus on increases in forthcoming ENSO rainfall and temperature fluctuations

89    under increasing GHG concentrations. The PDO, which is essentially the extra-tropical manifestation

90    of ENSO, is simulated with a similar spatial pattern as at present under various future climates but

91    with reduced amplitude and a shorter characteristic time scale (e.g., Zhang and Delworth, 2016).  The

92    North Atlantic is a key ocean for investigating global climate changes (Wang and Dong, 2010), and

93    acts as a major carbon dioxide sink (Watson et al., 2009). Atmospheric $CO_2$ concentrations vary with

94    the phase of the AMO with the warm phase associated with lowered atmospheric $CO_2$ (Wang and

95    Dong, 2010). The two NAO action points in the Icelandic low and the Azores high have been projected

96    to significantly intensify and shift northeastward by 10-to-20° in latitude and 30-to-40° in longitude

97    in response to global warming (Hu and Wu, 2004).

Stratospheric Aerosol Intervention (SAI), is a type of SRM that has been widely simulated by many global climate models (e.g., Kravitz et al., 2013), which is accompanied by changing in global circulations such as the NAO teleconnection pattern (Moore et al., 2014), and is known in various models to partially offset the decline in the Atlantic Meridional Overturning Circulation (AMOC; Xie et al., 2022). Undorf et al. (2018) simulated the North Atlantic SST cooling accompanied by the historical rise of stratospheric sulfate aerosol from North America and Europe dating back to 1850-1975. Gabriel and Robock (2015) is the only study to date that explores the effects of SAI in multiple models on the possible amplitude and frequency changes of El Niño/Southern Oscillation (ENSO). They concluded that changes in ENSO in the SAI simulations were either not present or not large enough to be captured by their approach, given the across-model variability issue. Thus, little is known about possible changes that future global climate change scenarios with artificial cooling may have on ocean-atmosphere climate indices. Recently, a novel set of SRM models have been globally complete with the state-of-the-art climate models: Community Earth System Model versions 1 and 2 (CESM1 and CESM2). These models have improved planetary boundary layer turbulence, aerosols, radiation, and cloud microphysics which should enable more reliable for the forthcoming global climate change projections (Mills et al., 2017).

We use the Geoengineering Large Ensemble Simulation (GLENS) with 20 members from a single model, the Community Earth System Model 1 (CESM1) with Stratospheric Aerosol Intervention (GLENS-SAI), to explore the possible changes in climate teleconnection patterns under future climate change scenarios. The models use the Representative Concentration Pathway (RCP) 8.5 high GHG emissions forcing state (Riahi et al., 2011) as a baseline and increase stratospheric sulfur injections through the century, to maintain global surface temperatures at 2020 levels. This produces an increasingly large signal-to-noise ratio through the 21st century. In addition, we use recent simulations (SSP5-8.5-SAI) with an updated model version (CESM2). For these simulations, the SSP5-8.5 GHG emissions scenarios were used as the GHG baseline on which SAI was performed. The two different model experiments show some surprising differences in the required sulfur injections and climate outcomes with and without SAI applications (Fasullo et al., 2020, Tilmes et al., 2020). Thus, even models from different generations in the same family can produce sufficiently different climates to explore a range of plausibly real climate impacts. The goal of this study is to identify robust features across the two model versions in the response of climate indices (ENSO, PDO, AMO and NAO) to GHG induced global warming and its compensation by SAI.

We employed empirical orthogonal functions and wavelet transforms to decompose time series and study the differences in the climate teleconnection patterns between the SSP5-8.5 and SSP5-8.5-SAI

131  scenarios. Since teleconnection patterns are emergent features of the non-linear, chaotic climate

132  system (Ghil et al., 2002), their underlying physical causes are complex and not necessarily the same

133  in any model as on the real planet. Hence, we assess the potential changes in temporal and spatial

134  characteristics of climate indices of AMO, NAO, ENSO, and PDO under both extreme warming GHG

135  scenarios and with SAI employed to mitigate those warmings while maintaining extreme GHG

136  concentration trajectories.

137

138  **2. Data and Methods**

139  **2.1. Models and scenarios**

140  We used two SAI models and scenarios: (1) CESM1 for GLENS-SAI and (2) CESM2 for SSP5-8.5-SAI.

141  The GLENS simulations were done by the Community Earth System Model version 1 (CESM1) with

142  the Whole Atmosphere Community Climate Model (WACCM) as the atmospheric system integrated

143  to land, ocean, and sea ice models (Mills et al., 2017). The resolution of atmospheric component is

144  $1.25°$ in longitude and $0.9°$ in latitude. A 20-member reference simulation for the RCP8.5 scenario

145  (Riahi et al., 2011) over the 2010–2030 period with three ensemble members (001 to 003)

146  continuing up to the end of the 21st century. GLENS-SAI is a 20-member ensemble of stratospheric

147  sulfur dioxide ($SO_2$) injection simulations, spanning 2020-2099. Each ensemble member was begun

148  in 2010 with small differences in their initial air temperatures, while their ocean, sea-ice, and land

149  temperatures were the same. Even before the start of the SAI injections in 2020, the fully coupled

150  model produced variability between the ensemble members due to its chaotic nature. Here, we use

151  all available members of the RCP8.5 and GLENS-SAI simulations, which extend until the end of the

152  21st century. For the analysis, we used monthly SST and sea-level pressure (PSL).

153  We also analyzed output from the NCAR Community Earth System Model version 2- Whole

154  Atmosphere Community Climate Model Version 6 (CESM2(WACCM6)). This model version was used

155  for performing the Coupled Model Intercomparison Project Phase 6 (CMIP6; Eyring et al., 2016)

156  simulations. Like GLENS, this SAI experiment is according to the high GHG emissions scenario, called

157  SSP5-85 in CMIP6, (SSP5-8.5-SAI) and limits mean global temperatures to $1.5°C$ above 1850–1900

158  conditions, which without SAI, is exceeded around the year 2020 in CESM2(WACCM6) under SSP5-

159  8.5. The experiment used sulfur injection locations at the same four latitudes as in GLENS to

160  accomplish the same three temperature goals (Tilmes et al., 2020). We used the monthly SST and PSL

161  data from all five members (r1 to r5) of the SSP5-8.5 scenario (covering 2015-2100) and the three

162  available ensemble members of SSP5-8.5-SAI that cover the period of 2020-2100. For the analysis,

163  we also applied a one-member historical simulation based on the specific CESM1(WACCM) version

164  used for GLENS between 1980-2009 (denoted as "historical" in the following). All three
165  corresponding members (r1 to r3) from the CESM2(WACCM6) version were used for the historical
166  period.

167  The SAI scenarios using both CESM1 and CESM2 inject $SO_2$ at four predefined points (30°N, 30°S,
168  15°N, and 15°S) at ~5 km above the tropopause using a feedback controller to maintain not just the
169  global mean temperature, but the interhemispheric and equator-to-pole temperature gradients.
170  Fasullo and Richter (2022) explain the inter-model differences in the aerosol mass latitudinal
171  distributions between the SAI experiments using CESM1 and CESM2. CESM2 SAI utilizes the CMIP6
172  SSP5-8.5 experiment as a baseline which has been used by various modeling teams (Tilmes et al.,
173  2020) while CESM1 SAI uses the well-known RCP8.5 scenario. In GLENS-SAI, most of the aerosols
174  were injected at 30°N and 30°S with much smaller injection mass at 15°N and a tiny amount at 15°S
175  while for SSP5-8.5-SAI, the highest concentrations were released at 15°S, modest mass at 15°N and
176  30°S, and a small amount at 30°N. These differences in the $SO_2$ distributions across the two SAI
177  scenarios for CESM1 and CESM2 produce a range of variability in shortwave radiation and cloud
178  responses to $CO_2$ concentration increases (Fasullo and Richter, 2022). Additionally, Fasullo and
179  Richter (2022) identified that changes in the spatial salinity and density patterns in the Atlantic
180  Ocean, and in turn, the Atlantic Meridional Overturning Circulation (AMOC), are very different under
181  GLENS-SAI compared to SSP5-8.5-SAI experiment. These differences between SAI simulations
182  represent part of the system variability.

183  The equilibrium climate sensitivity (ECS) of CESM2-WACCM is 4.75 °C and lies in an ECS range of 1.83
184  to 5.67 °C from 41 different CMIP6 GCMs (IPCC AR6, 2021). The absolute mean surface temperature
185  difference between CESM2-WACCM and historical records (0.89 °C) and is also within the range of
186  0.38-1.23 °C from 37 different CMIP6 models (Scafetta, 2021).  CESM2 is one of the best nine models
187  for simulating precipitation worldwide when measured by the Hellinger distance between bivariate
188  empirical densities of 34 CMIP6 models and the historical data from Global Precipitation Climatology
189  Centre (GPCC; Abdelmoaty et al., 2021). Additionally, the global-mean values of SST, summer land
190  temperatures, precipitation, and ECS simulated by CESM1 and CESM2 are roughly similar to each
191  other as well as compatible with the historical values over the 1985-2014 period (Danabasoglu et al.,
192  2020; Table S1).

193  Relative to the preindustrial 1851-1850 period, CESM2-WACCM projects global mean surface air
194  temperature rises of ~6.25 °C by the 2071-2100 period under SSP5-8.5 which compares with the
195  range of ~3.3-6.6 °C from 35 ensembles of 12 CMIP6 models (Cook et al., 2020).

196

## 2.2. Climate indices

The AMO was calculated from the area-weighted average of SSTs across the northern Atlantic from 0-70° N. The NAO was computed from the PSL time series at two stations: Gibraltar (to the south of Spain; around 36.1°N and 5.3°W) and Reykjavik (in the southwest of Iceland; around 64.1°N and 22.0°W). The ENSO index follows the definition proposed by Trenberth (1997). Here, we used SSTs at the Niño 3.4 region (east-central equatorial Pacific between 5°N-5°S, 170°W-120°W) as a proxy for ENSO. After removing the global mean SST anomaly, the leading Empirical Orthogonal Function (EOF) of monthly SST anomalies across the North Pacific (20°–70°N) is termed PDO following Mantua et al. (1997). All these computations were analyzed through the Climate Data Toolbox prepared by Greene et al. (2019). As an example, Fig. 1 compares AMO, NAO, ENSO, and PDO indices obtained from SSP5-8.5 and SSP5-8.5-SAI scenarios.

We characterized ENSO by El Niño and La Niña episodes. The ENSO index positive and negative episodes correspond to El Niño and La Niña, respectively. Consistent with Gabriel and Robock (2015), ENSO episodes were identified as departures of at least 0.5 standard deviations from zero in a five-month running averaged ENSO time series. Each episode was characterized by its duration (years), the extreme peak excursion (°C), and the width at half extreme height (years).

214
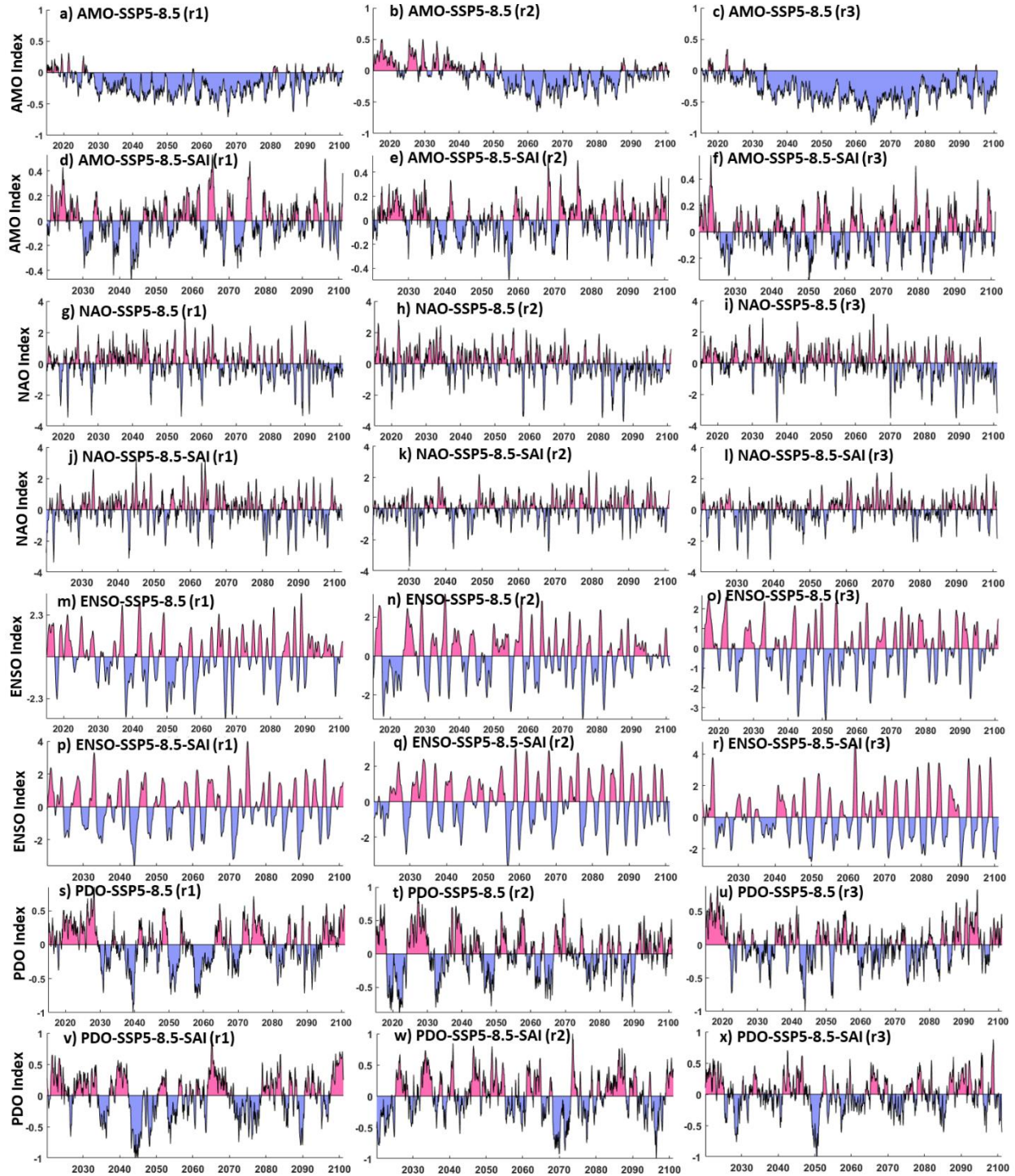
**Figure 1.** AMO (panels a-f), NAO (panels g-l), ENSO (i.e., NINO3.4, panels m-r), and PDO (panels s-x)

indices obtained from ensemble members r1(left column), r2 (middle column), and r3 (right

column) of the SSP5-8.5 (odd rows) and SSP5-8.5-SAI (even rows) scenarios.

218

219

## 2.3. Spatiotemporal analyses

Analyses in both space and time as well as modes of variability ranging from the inter-annual through decadal, to inter-decadal changes were used to identify the possible changes in the large-scale climate circulations resulting from global warming and SAI scenarios. EOF analysis is commonly used to extract the climate variability space-time modes (e.g., Chen and Tung, 2018; Joyce, 2002). We applied EOF to extract the first (dominant) modes of de-trended non-seasonal-SST and its corresponding variance across the North Atlantic and North Pacific, which are related to the AMO and PDO respectively. As ENSO is the primary indicator of global climate variability, we used the leading EOF of global SST anomalies in the study of ENSO.

The continuous wavelet transform (CWT) is commonly used to capture the primary characteristics of signals (Addison, 2018). For a time series ($x_n$, $n$=1, . . . , $N$) having regular time intervals $\delta t$, the CWT is computed as the convolution of $x_n$ with the scaled and normalized wavelet (e.g., here we use the Morlet wavelet which gives reasonably equal weighting and resolution in time and period space; Grinsted et al., 2004):

$$W_n^X(s) = \sqrt{\frac{\delta t}{s}} \sum_{n'=1}^{N} x_{n'} \psi_0 \left[ (n'-n)\frac{\delta t}{s} \right] \text{ where } \psi_0(\eta) = \pi^{-1/4} e^{i\omega_0 \eta} e^{-0.5\eta^2} \tag{1}$$

where $s$ is the wavelet scale, $\psi_0$ the Morlet wavelet, $\omega_0$ dimensionless frequency, [*] the complex conjugate, and $\eta$ dimensionless time. The noise spectrum assigned to generate significance testing is a key issue in time series analysis. We concurred with the widely-used red-noise null hypothesis methodology based on 1000 synthetic series with the same mean, standard deviation and first-order autoregressive coefficient as the target time series produced by Monte Carlo approaches to estimate the significance of the CWT (Grinsted et al., 2004). Additionally, for each time series, CWT's global power spectrum was calculated as a function of time. The global power spectrum provides insight into the dominant temporal modes of variability of each climate index within each ensemble member for the reference GHG and SAI scenarios. The wavelet method cone of influence automatically shows where the periods analyzed are being influenced by the end of the time series. Thus, the longest periods can only be reliably assessed for the middle of the time series.

The individual ensemble members are treated as independent of each other in calculating the statistics of the ensembles. The CWT was conducted on monthly ENSO time series, and the 12-month moving averaged low-pass filtered signals of AMO, NAO, and PDO. We always use the longest available record length in every ensemble member to gain maximum statistical power to establish significant differences between experiments.

**3. Results:**

**3.1. Changes in the spatial patterns**

Figure 2 reveals the projected changes in the variance of the SST anomalies related to the AMO (i.e., across the North Atlantic), ENSO (i.e., global scale), and PDO (i.e., across the North Pacific) based on CESM1 and CESM2 results. Figure S1 shows three different plots for the CESM1 as the time period of the 20-member ensemble for RCP8.5 differ: ensembles 001 to 003 (2010-2097) are longer than the other 17 ensemble members (2010-2030). For RCP8.5 and SSP5-85 using CESM1 and CESM2, respectively, the strong GHG forcing and global warming to the end of the 21$^{st}$ century increases the variance of the first EOF SST anomaly in the North Atlantic and North Pacific (representing AMO and PDO), but reduces the variance of the leading EOF in global SST anomaly (related to ENSO). Based on the statistical t-test results, the changes in the means imposed by global warming relative to historical are all significant except one case (Fig. 2f). Differences between SAI and historic in CESM2 values of the leading EOF variance of AMO and ENSO are not significant, showing that the significant changes under GHG forcing are effectively reversed by SAI. In contrast, the changes in PDO variance imposed by global warming using CESM1 relative to historical remain significant under SAI. Using CESM2, there is no significant changes in the PDO variance from historical to global warming, or to SAI.

268
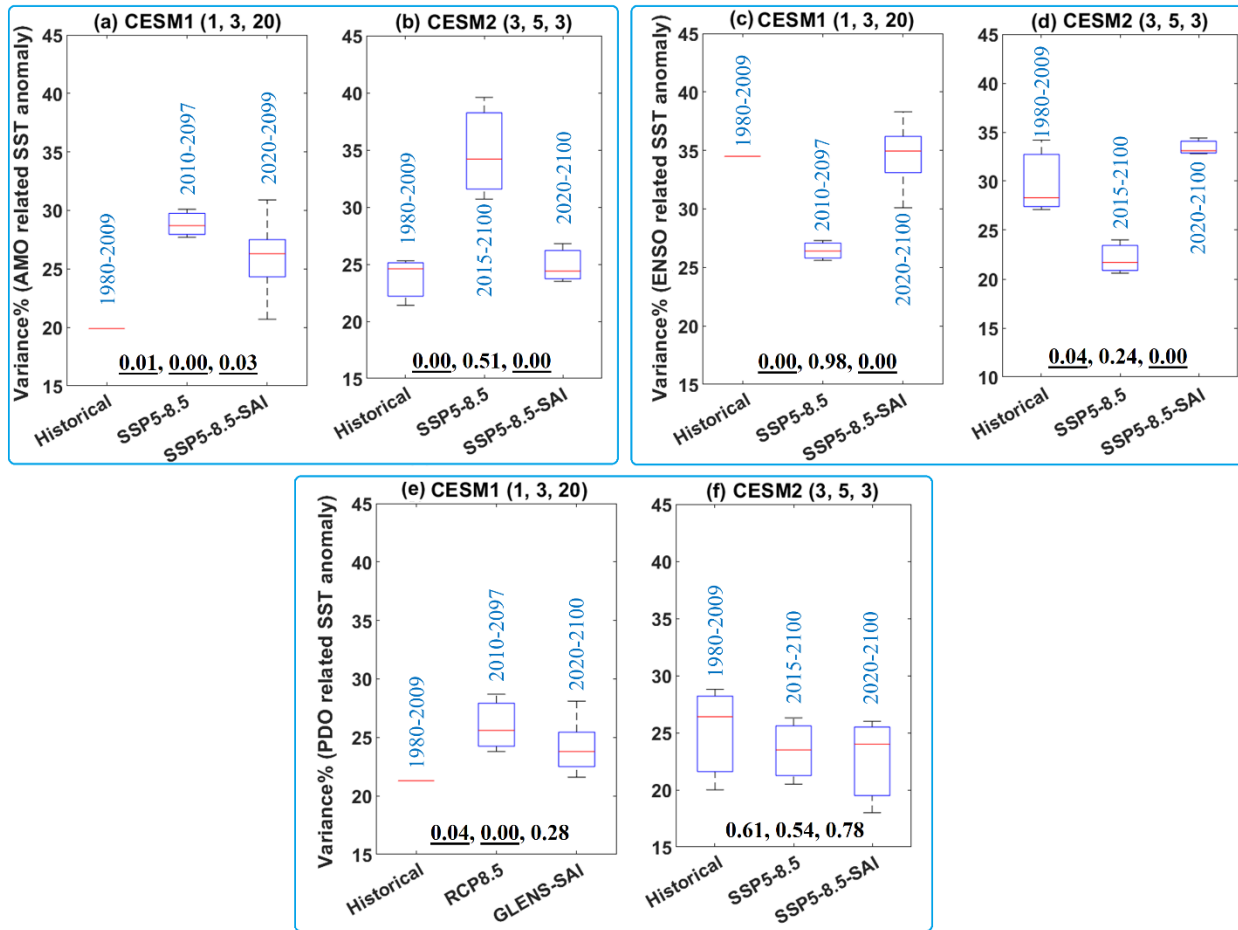
**Figure 2.** Box and whiskers plot of the variance in the leading EOFs, representing AMO, PDO, and ENSO, relative to the total variance of the SST fields: AMO across the North Atlantic (top-left panel); ENSO (top-right panel) global SST; and PDO across the North Pacific (bottom panel). The values in blue on each column box show the period of the data for historical, GHG (i.e., RCP-8.5 and SSP5-8.5), and climate intervention (GLENS-SAI and SSP5-8.5-SAI) scenarios. The titles of each subplot refer to the CESM version and the number of ensembles used in the historical, GHG (RCP8.5 and SSP5-8.5), and SAI (GLENS-SAI or SSP5-8.5-SAI) scenarios, respectively. The median for each experiment is denoted by the red line, the upper (75th) and lower (25th) quartiles by the top and bottom of the box and ensemble limits by the whisker extents. The three values shown at bottom of each sub-plot refer to the p-values obtained from the statistical t-test between historical and global warming, historical and SAI, and global warming and SAI, respectively. Values underlined are significant (i.e., $p < 0.05$)

Figures 3-6 and S2-S3 show the spatial anomalies of the leading EOF mode of the SST in the North Atlantic, North Pacific, and tropical pacific under both the CESM1 and CESM2. For the historical period, there is a cold-tongue pattern in the North Pacific broadens from the western to the eastern parts surrounded by warm water, particularly to the north. GHG related global warming lowers the contrast between the cold-tongue pattern and its surroundings and increases the water temperature inside the cold-tongue-pattern, and also leads to a substantial expansion of a warm-pattern in the

288   north. The same patterns (Fig. 4) are also obtained under SSP5-8.5 using CESM2. SAI effectively

289   shrinks the warm pattern in the northern Atlantic under the RCP8.5 and SSP5-8.5 through a

290   significant SST decrease, particularly using CESM1 (bottom row in Figs. 3 and 4). The SSP5-8.5-SAI

291   experiment increases the temperature contrast in the cold-tongue pattern, while the GLESN-SAI does

292   not. The projected changes in the spatial SST patterns across the North Atlantic, observed under

293   global warming, are significantly suppressed under SAI (Figs. 3f and 4f). This response of AMO to SAI

294   is compatible with the observed changes in AMO imposed by anthropogenic and volcanic aerosols

295   reported by Masson-Delmotte et al. (2021). Anthropogenic and volcanic aerosols are understood to

296   have impacted the timing and magnitude of the cold (negative) episode in the historical AMO record

297   between the mid-1960s and mid-1990s and succeeding warming (Masson-Delmotte et al., 2021).

298   Anthropogenic aerosols have also been suspected as impacting historical SSTs elsewhere,

299   particularly the decadal ENSO variability (e.g., Sutton and Hodson, 2007; Westervelt et al., 2018).

300
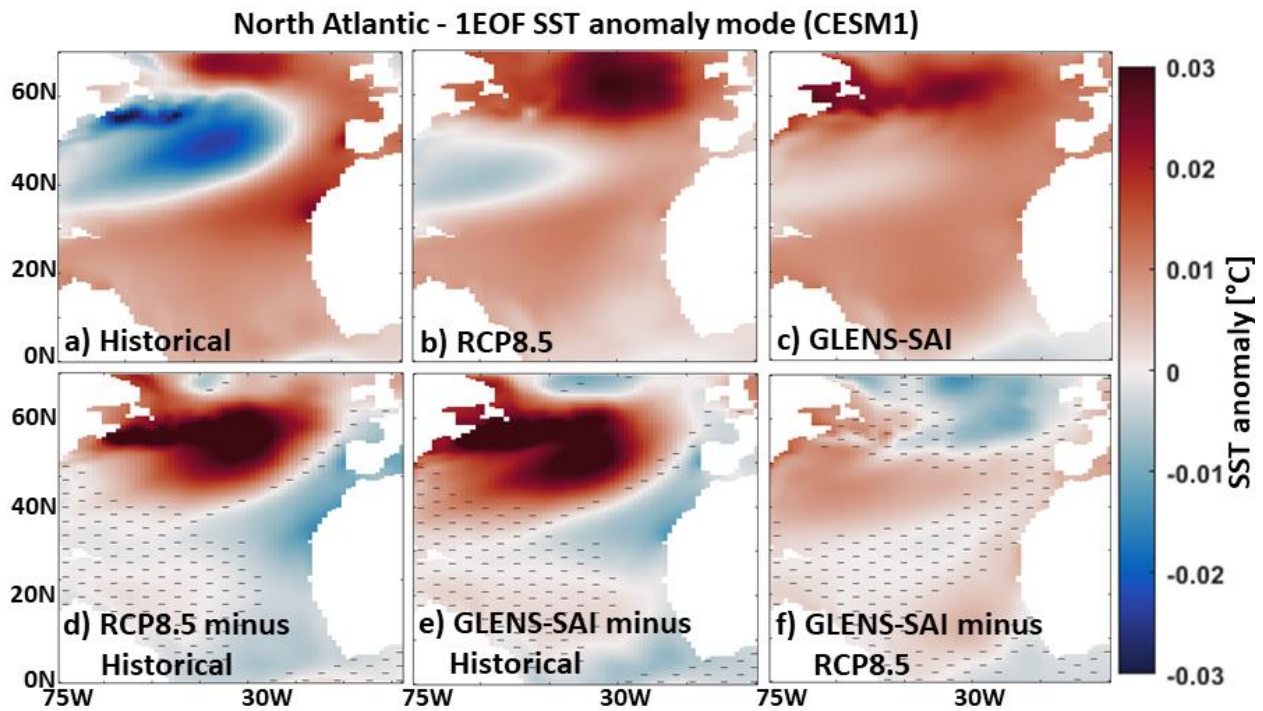
302   **Figure 3.** The first EOF (1EOF) patterns of SST anomaly across the North Atlantic relate to the AMO
303   index simulated by CESM1 for the historical data (a) and the mean of the available ensemble
304   members outputs under the RCP8.5 (b) and GLENS-SAI (c) scenarios. The maps at the bottom row
305   show RCP8.5 minus historical (d), GLENS-SAI minus historical (e), and GLENS-SAI minus RCP8.5 (f)
306   where the hatched patterns are not statistically significant (p>0.05), based on p-values from t-test
307   analysis.

308
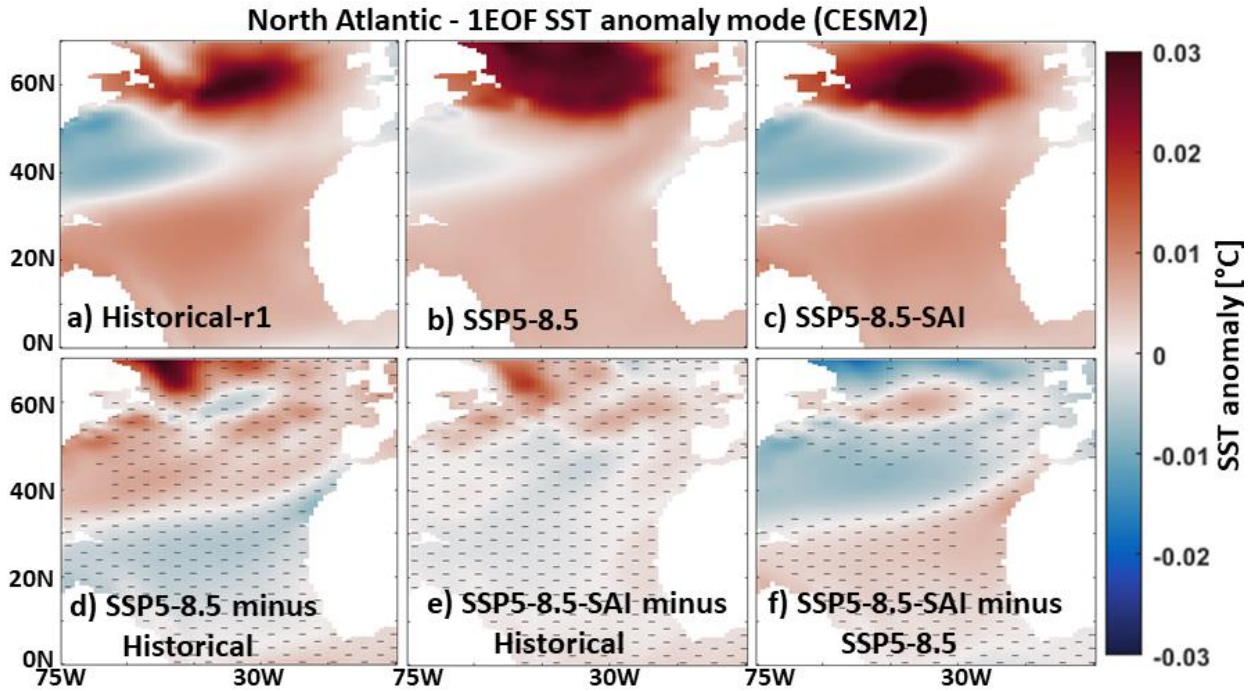
309 **Figure 4**. As in Fig. 3, but for CESM2 and SSP5-8.5.

310

311 The leading EOF of monthly global SST anomalies corresponding to the ENSO mode (Figs. S2 and S3),

312 and is seen as a warm-tongue pattern over the tropical Pacific, that exhibits very similar patterns

313 under both global warming and SAI scenarios as in the historical period. However, Fig. S4 shows that

314 the warm-tongue pattern in CESM1 and CESM2 has an excessive westward extension relative to

315 observations, which is compatible with the findings of Capotondi et al. (2020).

316 While the first EOF SST anomaly across the North Pacific under both global warming and SAI

317 scenarios in CESM1 and CESM2 (Figs. 5 and 6) exhibits a similar cold-tongue pattern (typical of the

318 North Pacific) as in the historical period. A lower contrast between the cold-tongue pattern and its

319 surroundings is observed under SSP5-8.5 (Fig. 6b), which is effectively compensated by the

320 geoengineering scenarios of SSP5-8.5-SAI through a significant SST decrease over middle North

321 Pacific (Fig. 6c and 6f) since there is no significant change between SAI and historical maps (Fig. 6e).

322 There is an excessive eastward expansion of the cold-tongue pattern with cooler temperatures under

323 the SAI scenario as simulated by the CESM1 (Fig. 5c), which is due to the significant cooling of the

324 water in the outside of the cold-tongue pattern imposed by the $SO_2$ injection (Fig. 5e-f).

325

326
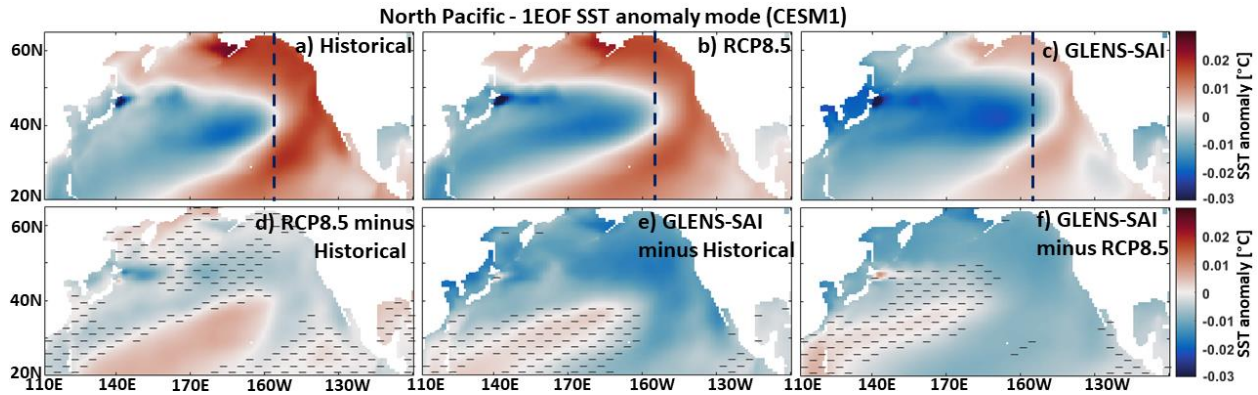
**Figure 5**. As Fig. 3 but across the North Pacific relates to the PDO index.
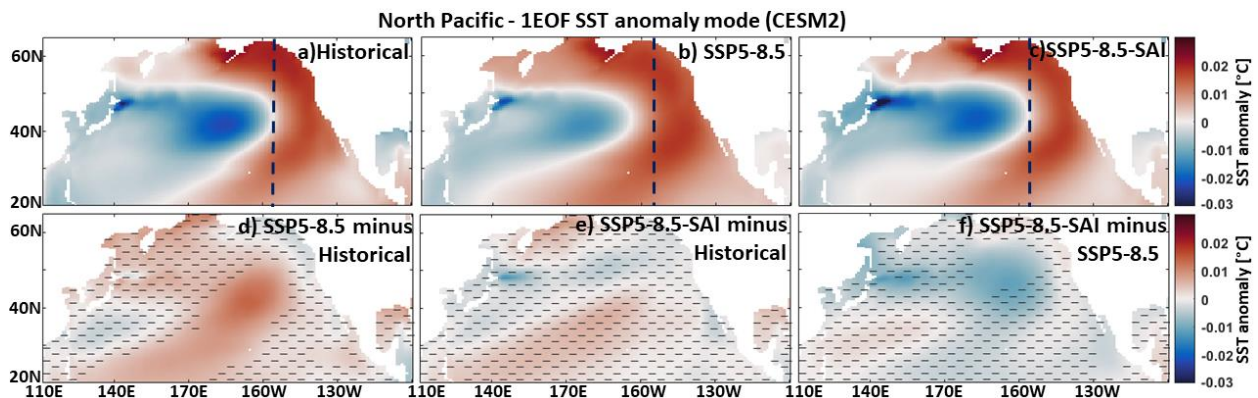
**Figure 6**. As in Fig. 5, but for CESM2.

## 3.2. Temporal evolution of indices

Figure 7 displays the projected changes in the El Niño and La Niña episodes in the ENSO index under global warming and SAI. The global warming scenario simulated by CEMS2 tends to reduce the time between, as well as the intensity and duration of the La Niña episodes compared to the historical conditions, but El Niño shows no significant changes. Frequency increases in both El Niño and La Niña episodes were suggested in earlier climate simulations e.g., Fredriksen et al. (2020), Cai et al. (2014) and Yun et al. (2021) for El Niño, and Cai et al. (2015) for La Niña. In contrast, using CESM1, the characteristic changes of El Niño are stronger than that of La Niño and the El Niño intensity significantly increases while its duration decreases relative to historical period. The La Niña intensity significantly increases but other characteristics show no significant changes under RCP8.5.

For CESM2, although the SAI is mostly accompanied by a slight decrease in the median of El Niño/La Niña characteristics towards their historical value, its effect on global warming imposed-changes is only statistically significant for the intensity and duration of La Niña events. For the CESM2 SAI

346 experiment, there are no significant differences in El Niño characteristics as with the GHG forcing
347 experiment. In contrast La Niña peak intervals, height (i.e., intensity), and width (i.e., duration)
348 characteristics are significantly different from GHG forcing and reverse the direction of changes
349 imposed by GHG. For CESM1, there are no significant differences between the results from RCP8.5
350 and GLENS-SAI scenarios.
351
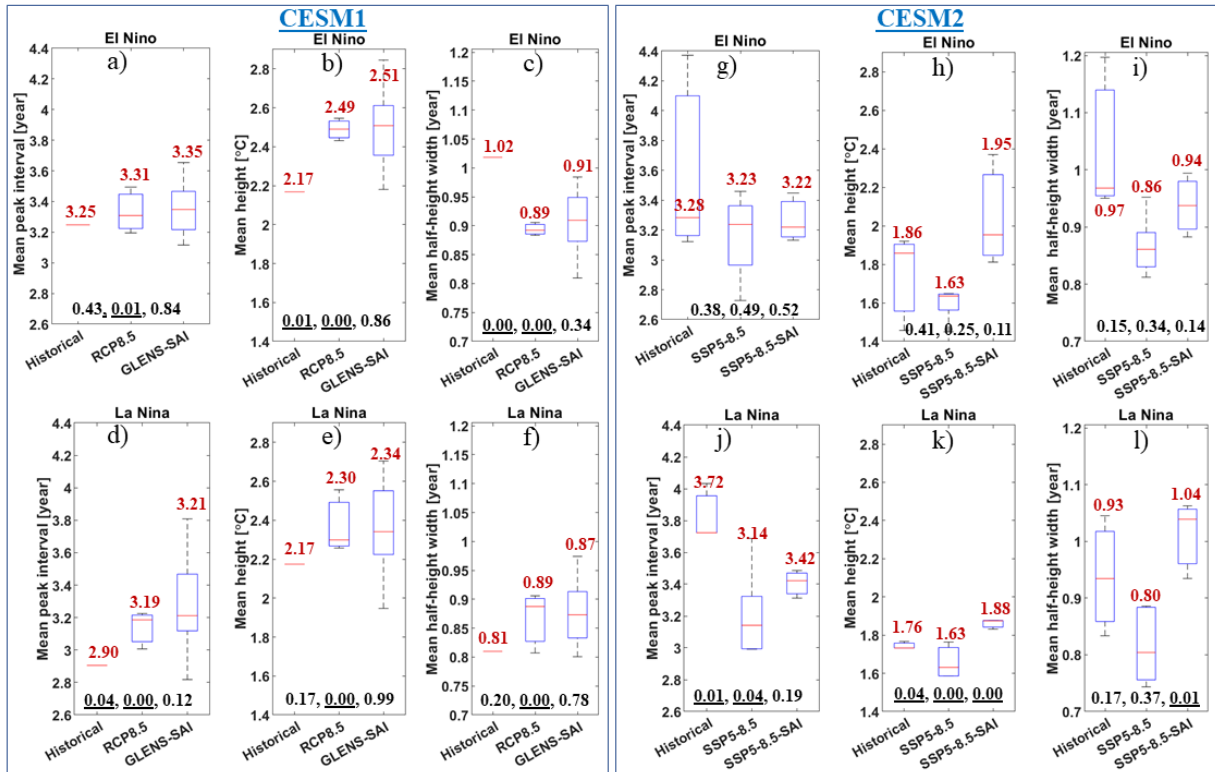
353 **Figure 7.** The projected changes in the mean peak interval, height, and half-height width of El Niño
354 and La Niña events for global warming (RCP8.5 and SSP5-8.5) and SAI (GLENS-SAI and SSP5-8.5-
355 SAI) scenarios simulated by CESM1 (panels a-f) and CESM2 (panel g-l). The median for each
356 experiment is denoted by the red line, the upper (75th) and lower (25th) quartiles by the top and
357 bottom of the box and ensemble limits by the whisker extents. The values labeled in red on each
358 box show their median. The three values shown at bottom of each sub-plot refer to the p-values
359 obtained from the statistical t-test between historical and global warming, historical and SAI, and
360 global warming and SAI, respectively. Values underlined are significant (i.e., $p<0.05$).
361
362 Another way to illustrate the temporal evolution of signals is by using the power spectrum. Figures
363 8 and S5 compare the changes in temporal variability of each climate indices (AMO, NAO, ENSO, and
364 PDO) using the global power spectrums of CWTs under the global warming and SAI scenarios
365 simulated by CESM2, excluding CESM1 outputs as there is just a single ensemble member for CESM1
366 historical data over a short 1980-2009 period. In CESM1, the signals longer than 25 years, which are
367 the most energetic modes in observations of the PDO (Mantua and Hare, 2002) and AMO (Enfield et

368    al., 2001), cannot be captured in the historical simulations owing to their short simulation period
369    (1980-2009). As an example, Fig. S5 shows the ENSO CWTs and their global power spectrums for
370    historical, SSP5-8.5, and SSP5-8.5-SAI scenarios.
371    The inter-annual modes of AMO, NAO, and ENSO are preserved under both global warming and SAI.
372    For the decadal and longer periodicities, SAI accentuates AMO changes induced by GHG (Fig. 8a). For
373    example, the dominant modes at 20-30- and 55-85-year of the AMO, observed during the historical
374    period, show no significant changes under global warming; however, they vanish under SAI. The
375    decadal 10-20-years mode of the historical NAO is not preserved in the global warming scenario nor
376    with SAI (Fig. 8b). For ENSO, the dominant historical inter-annual modes show no significant change
377    under both global warming and SAI, except that its power under SAI is stronger (Fig. 8c). The
378    dominant modes at 10-20- and 50-70-years, observed in historical PDO (consistent with the real
379    PDO's dominant modes (Mantua et al., 1997)), are not present in both the SSP5-8.5 and SAI
380    simulations, and the latter two are similar to each other (Fig. 8d). In contrast with the historical
381    period in which the dominant modes of PDO occur in the 10-20- and 50-70-year bands, the dominant
382    modes under global warming (i.e., SSP5-8.5) and SAI (i.e., SSP5-8.5-SAI) occur at the ~10-year period.
383    The PDO shift to a higher frequency with decadal/multi-decadal variability weakness, observed
384    under global warming, was also earlier demonstrated by Fang et al. (2014) with a previous
385    generation of the climate model, the Fast Ocean Atmosphere Model (FOAM) used in IPCC AR4
386    experiments. Likewise, the PDO timescale has been simulated to decrease from ~20 to ~12 years
387    under global warming (Fedorov et al., 2020), possibly because of changes in the phase speed of
388    internal Rossby waves and ocean stratification (Zhang and Delworth, 2016). Nonetheless, although
389    PDO cycles between 30-50-year bands show slightly stronger power under SAI than global warming,
390    the 30-50-year is not the dominant PDO mode under SAI in contrast to Zhang and Delworth's (2016)
391    results for cooler climates, which the PDO dominant variability shifts to lower frequency (~34 yr).
392    They related this increase to weaker ocean stratifications accompanied by global cooling. However,
393    Zhang and Delworth (2016) used a different model (Geophysical Fluid Dynamics Laboratory coupled
394    model version 2.5 through the forecast-oriented low ocean resolution version) and experiments
395    ($2 \times CO_2$ for global warming and $0.5 \times CO_2$ for cooling).
396    We further analyzed the concatenated series from the available members for each scenario using
397    CESM2 to statistically capture the low frequency cycles with better reliability. Figure S6 summarizes
398    the CWT global power spectrums for AMO, NAO, ENSO, and PDO. The results, on the whole, are
399    compatible with those shown in Fig. 8, despite small discrepancies such as the much stronger
400    interdecadal mode in AMO obtained from the concatenated ensembles.
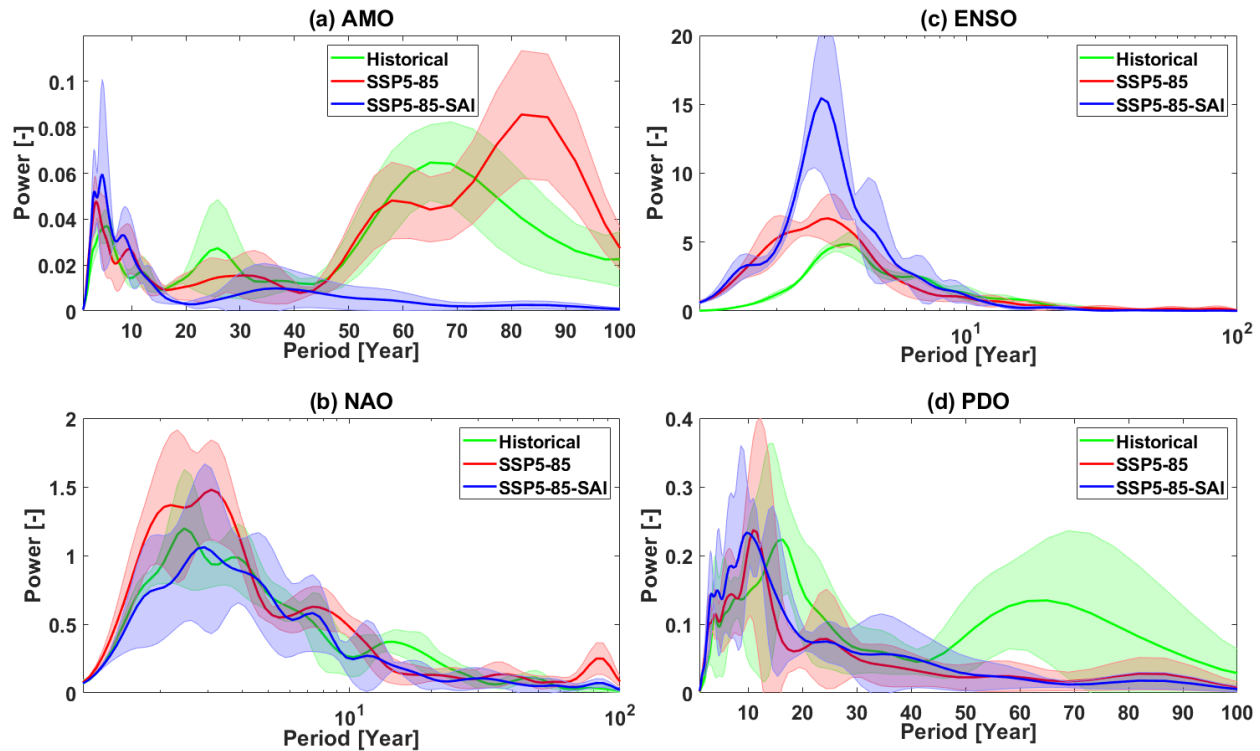
**Figure 8.** The CWT global power spectrums obtained for the indices of AMO (a), NAO (b), ENSO (c), and PDO (d) under SSP5-8.5 and SSP5-8.5-SAI relative to the historical results based on CESM2 for the periods of 1850-2014. Shading in each curve shows the across-ensemble range. The x-axis in NAO and ENSO graphs is on logarithmic scale.

## 4. Discussion

### 4.1. Caveats to interpretation

Caution is required when interpreting the results from this study with regard to real-world variability. Although CESM2 is highly rated among existing climate models, large model–observation differences are nonetheless present (Fasullo, 2020). Model-observation differences are larger in the earlier CESM1 version than in CESM2. For example, CESM1 exhibited a Subtropical (Azores) high anomaly (related to NAO) that was too weak but its representation is improved in CESM2 (Simpson et al., 2020). We also find large differences in amplitude and variance of climate indices simulated by both CESM1 and CESM2 relative to the observations over the 1980-2009 period. The amplitude of the dominant EOF of the ENSO-related SST-anomaly modeled in both CESM1 and CESM2 is about twice the observations for the historical (1980-2009) period (Figs. S4 and S7). Figure S7 further shows NAO and PDO dominant mode amplitudes are lower in the model projections than in observations over the historical period. Additionally, the ENSO-associated SST anomaly pattern in the tropical Pacific shows an excessive westward extension under both CESM1 and CESM2 (Fig. S4).

421    These limitations mirror those by Capotondi et al. (2020) for CESM2 in simulating the ENSO, who

422    suggested further work to illuminate how the physical parameterizations impact the key ENSO

423    feedback. Additionally, although CESM2 simulates the pattern of the summer and winter NAO well

424    over the historical period 1979-2014, the large uncertainties in specific members and in the historical

425    observations mean it is difficult to be quantitative about this (Simpson et al., 2020). However, CESM1

426    tends to underestimate the observed SST fluctuations in the Atlantic, leading to an underestimation

427    of the forced response (Undorf et al., 2018).

428    CMIP models tend to systematically underestimate the low-frequency signals (i.e., PDO) in the North

429    Pacific (Fasullo et al., 2020), owing in part to an imperfect modeling of decadal-scale structures in

430    these simulations (Masson-Delmotte et al., 2021). Compared to observational estimates, the decadal

431    variability in the subpolar North Atlantic SST appears to be slightly intensified through CMIP6

432    (Masson-Delmotte et al., 2021). How well we, therefore, can potentially capture forthcoming changes

433    in climate indices' variability will be restricted by how good each model simulations are (Gabriel and

434    Robock, 2015).

435    The second limitation is disparities in the length of records (30 years for the historical period, roughly

436    90 years for GHG emissions, and 80 years for SAI scenarios) may hinder the direct comparison of

437    climate indices behavior between historical and future climate scenarios of global warming and SAI;

438    and thus, the number of El Niño/La Niña events as well as the significance of the longer periodicities

439    (i.e., decadal and inter-decadal) in power spectrums. Furthermore, these records explore variability

440    within the statistical assumptions of the methods, which may not be robust for non-stationary time

441    series where the Normality and independence assumptions inherent in the wavelet and t-tests would

442    not strictly hold. We are limited to the available simulations, and a 3-member ensemble for SAI under

443    CESM2 is inherently weaker than 20-member ensembles under CESM1. CESM1 has a shorter 30-year

444    historical period from 1980 to 2009 which could not capture the interdecadal variability modes of

445    the teleconnection patterns. Yet another limitation arises from the relatively low spatial resolution

446    of the models which may affect the spatial SST anomaly patterns. Furthermore, Holmes et al. (2019)

447    pointed out the models are too low resolution to resolve ocean eddies, which substantially contribute

448    to ENSO irregularity and predictability. The absence of the eddy process may also be associated with

449    bias in spatial patterns and other ENSO characteristics (Bellenger et al., 2014) in the CMIP models

450    (Cai et al., 2021). Global high-horizontal resolution climate models have been indicated to

451    significantly improve the ocean-atmosphere circulations such as ENSO (Masson et al., 2012). As an

452    example, Haarsma et al. (2016) pointed out that the High Resolution Model Intercomparison Project

453    for CMIP6 improves the understanding of the climate teleconnection patterns of large-scale

454    circulations such as ENSO, NAO, and PDO, which suggests that running these high-resolution models

455    with SAI scenario would be worthwhile.

456

457    **4.2. Implications for climate stability**

458    Teleconnection signals represent emergent properties of the non-linear climate system. The

459    behavior of the climate teleconnection patterns can be characterized via its oscillations. In its

460    simplest form, a stable pattern would represent a fixed point or a periodic oscillation, but with real

461    non-linear systems, a quasi-periodic oscillation over specific frequency bands is more likely (e.g., Ghil

462    et al., 2002). These quasi-periodic characteristic frequencies may change smoothly over time in a

463    linear system but may proceed towards chaotic solutions via frequency doubling in non-linear

464    systems. Moron et al. (1998) suggested that ENSO crossed a threshold in the early 1960s, and the

465    periodicity of the seasonally forced climatic oscillator increased abruptly. The notable decline in low-

466    frequency multi-decadal band components of the wavelet spectra of the indices we study,

467    accompanied by a concomitant increase in the variance of the decadal band is consistent with abrupt

468    frequency doubling. This can be expected in non-linear systems as the energy in the system is raised,

469    progressing along the pathway towards chaotic behavior and hence less predictability on decadal

470    timescales.

471    The impact of SAI on the energetics of the coupled system are to offset the GHG increases by design.

472    Hence, we might expect that SAI could therefore reduce or stop the progression towards chaotic

473    behavior. However, the real climate system is far more complex than a simple energy balance

474    calculation. SAI increases stratospheric heating (Visioni et al., 2020), and this leads to tropospheric

475    changes, especially in winds (Gertler et al., 2020), and tropical circulation (Cheng et al., 2022).

476    Furthermore, the large heat reservoir of the global ocean has been out of equilibrium with the

477    atmosphere for centuries of anthropogenic GHG emissions, and this excess heat cannot be dissipated

478    by SAI within the timeframe in the simulations. So, we may expect SAI to, at best, imperfectly reverse

479    the effects of GHG on teleconnections.

480    Ocean stratification (ocean buoyancy frequency) and the baroclinic Rossby wave in the North Pacific

481    play significant roles in SST amplitude and PDO cycles since enhanced ocean buoyancy frequency

482    speeds up the Rossby waves, and so the decadal and longer cycle weakening accompanies higher PDO

483    frequency (Fang et al., 2014). Ocean stratification changes predominantly in response to changes in

484    surface temperature and salinity (Fang et al., 2014). The North Atlantic and the northeast Pacific are

485    projected to be among those areas with the greatest stratification changes under global warming in

486    the second-half of the 21st century (Capotondi et al. 2012). Historical records also show that volcanic

487   sulfate aerosols have altered multi-decade SST variability in the North Atlantic and North Pacific

488   (Birkel et al., 2018).

489   While SAI effectively reverses the changes in the spatial patterns under GHG forcing across the North

490   Atlantic (i.e., AMO) and North Pacific (i.e., PDO) and compensates for modest changes in the

491   characteristics of the El Niño and La Niña episodes (related to the tropical Pacific), it does not

492   effectively suppress the projected changes in decadal (~10-20-year) and inter-decadal (longer than

493   ~20-year) variability of circulations imposed by global warming. Anthropogenic aerosols intensify

494   the inter-annual variability (particularly in ENSO) but weaken the longer than 10-year signals of the

495   ocean-atmosphere circulations, compatible with the multiyear to decadal variations in PDO (Hua et

496   al., 2018). SAI involves aerosols in the stratosphere not the troposphere, so the effects will be

497   different, not least because of stratospheric heating (Visioni et al., 2020). The cold-tong pattens in the

498   mid-latitude of both North Atlantic and North Pacific tend to have an excess eastward extension

499   under SAI, in line with the second-phase of the North Pacific response to large volcanic eruptions

500   (Wang et al., 2012), which are better analogues for SAI.

501   Whether the climate system in the model is representative of the earth can be diagnosed to some

502   extent by comparison of the historical simulation with observations. As noted in Section 4.1 both

503   CESM versions do present differences from observations, so they are not perfect. All climate models

504   are unavoidably uncertain (Knutti et al., 2002), mostly because of the imperfect understanding of

505   many of the interplays and feedbacks within the climate system (Jun et al., 2008). Previous analysis

506   of ENSO under SAI found no significant changes (Gabriel & Robock, 2015), but they used different

507   models with widely varying fidelity of modeled ENSO to observations, and much smaller simulated

508   quantities of $SO_2$ with the relatively modest RCP4.5 emissions scenario as a baseline. Furthermore,

509   in the only previous assessment of ENSO under SAI, by Gabriel and Robock (2015), SAI simulations

510   may not have been long enough to detect changes. The large 20-member ensemble of GLENS used in

511   this study may overcome this limitation, especially for short-period indices, since this represents

512   ~1600 model-years.

513   Changes in climate teleconnection patterns can indicate significant changes in the forcing. Such

514   changes are seen in time series analysis of teleconnection indices in the real world that coincide with

515   increased GHG (Tsonis et al., 2007; Wang et al., 2009). Wang et al (2009) note that regime shifts in

516   system behavior in the observations occurred when North Pacific and North Atlantic patterns

517   increase their coupling, and the key instigator is the NAO. The NAO's long-period counterpart, the

518   AMO, are seen in our simulations to change under SAI relative to GHG forcing at periods longer than

519  a decade. The historical NAO's decadal mode which vanished under global warming is not restored
520  by the simulated SAI.

521  The North Atlantic is an atypical region under SAI. The declines in heat transported northwards by
522  the AMOC under GHG forcing are, to great extent, reversed under all kinds of SRM including SAI (Xie
523  et al., 2022). Thus, great differences exist in SST and air/ocean heat flux between SAI and GHG
524  climates in the North Atlantic (Yue et al., 2021). If regime shifts occur when North Atlantic and Pacific
525  oceans increase their coupling, and if the decline in AMOC under GHG forcing decreases coupling
526  between the basins, then SAI may act to promote regime shift by reversing a decline in AMOC.

527  Many authors have noted that explosive volcanism, in some ways a natural analogue for SAI, is
528  accompanied by a positive episode of the NAO (e.g., Robock, 2000), and this may then be associated
529  with changes in multi-decadal AMO variability (Birkel et al., 2018). Furthermore, in the extreme
530  scenario of SAI being done such that temperatures are actually decreased then projected
531  strengthening of AMOC occurs (Tjiputra et al., 2016). However, it is also possible that regime shifts
532  induced by GHG forcing and the large temperature feedbacks they induce may dominate impacts over
533  those fairly subtle regime shifts in climate teleconnection patterns.

534

535  **5. Conclusions**

536  This study delivers a first overview of SAI response on the large-scale ocean-atmosphere circulations
537  of AMO, NAO, ENSO, and PDO using experiments based on CESM1(WACCM) and CESM2(WACCM6)
538  that apply stratospheric aerosol intervention through the injection of sulfur into the stratosphere,
539  GLENS-SAI and SSP5-8.5-SAI, respectively. The impacts of these interventions are assessed against
540  historical (1980-2009 for both the models and 1850-2014 for CESM2 in some analyses) and
541  projections under RCP8.5 and SSP5-85 (for the GLENS-SAI and SSP5-8.5-SAI, respectively). We found
542  that SAI effectively reverses the global warming-imposed changes in the variance of the leading EOF
543  SST anomaly associated with AMO, ENSO, and PDO. The SAI also effectively suppresses the changes
544  in the spatial patterns of the EOF SST anomaly across the North Atlantic (i.e., AMO) and North Pacific
545  (i.e., PDO). A decrease in the contrast between the cold-tongue pattern and its surroundings in the
546  North Pacific is further projected under GHG induced global warming, which the SAI successfully
547  restored.

548  CESM2 simulations suggest that increasing GHG emissions are accompanied by a modest increase in
549  the frequency of the El Niño and La Niña episodes but a modest decrease in their intensity and
550  duration. The SAI scenario effectively compensates for these changes.

551  In contrast to the impact of the SAI on the spatial patterns of the climate indices of AMO, PDO, and

552  ENSO, the SAI scenario does not effectively suppress the projected changes in decadal (~10-20-year)

553  and inter-decadal (longer than ~20-year) variability imposed by global warming. The decadal and

554  inter-decadal variability modes of all the historical climate indices (except for Atlantic-based indices

555  under SSP5-8.5) are not preserved in the GHG warming scenario and the SAI does not restore them.

556  Furthermore, compared to the historical 1850-2014 period in CESM2, SAI is projected to accentuate

557  AMO and have no effective impact on NAO at decadal and longer frequencies. Unlike the historical

558  period in which the long-period dominant modes of PDO occur in the 10-20- and 50-70-year bands,

559  the dominant modes under global warming are reduced to ~10-years, and the SAI does not restore

560  them.

561  The results exhibited here are particular to these types of future global warming scenarios and the

562  details of the SAI application, which deal with an extreme scenario of GHG emissions and continuous

563  increases in sulfur emissions. Furthermore, the findings are from ensemble members from just two

564  closely related models. Caution is warranted due to the model-observation differences, disparities in

565  the record length of the historical period compared to future climate scenarios, and the low spatial

566  resolution of the models. Nevertheless, our study does detect changes in climate teleconnection

567  signals, and hence underlying climate system dynamics under SAI when decomposed using EOF and

568  wavelet analyses.

569

570  **Acknowledgments:**

571  We appreciate the financial support from The World Academy of Sciences (TWAS) under grant no:

572  4500443035. We further thank Gary Strand from NCAR for his help in accessing the CESM1 model

573  outputs. Tan Mou Leong provided helpful comments and suggestions on the manuscript.

574

575  **Competing interests:**

576  We confirm that there is no conflict of interest among the authors of this manuscript.

577

578  **Data availability:**

579  The data for CESM1 and CESM2 simulations are publicly available via their websites:

580  http://www.cesm.ucar.edu/projects/community-projects/GLENS/ (DOI: 10.5065/D6JH3JXX) and

581  https://esgf-node.llnl.gov/search/cmip6/.

582

583

584 **Author contribution:**

585 A. R.: Coordinated to analysis and the graphics of various figures and the manuscript preparation; Kh.

586 K. and S. T.: conceptualization and preparing the data; J. M. conceptualized and coordinated the

587 interpretation and discussion for various sections. All authors contributed to the discussion and

588 writing.

589

590 **References**:

591 Addison, P. S.: Introduction to redundancy rules: the continuous wavelet transform comes of

592        age, Philosophical Transactions of the Royal Society A: Mathematical, Physical and

593        Engineering Sciences, 376(2126), 20170258, https://doi.org/10.1098/rsta.2017.0258,

594        2018.

595 Abdelmoaty, H. M., Papalexiou, S. M., Rajulapati, C. R., and AghaKouchak, A.: Biases beyond the mean

596        in CMIP6 extreme precipitation: A global investigation, Earth's Future, 9(10),

597        e2021EF002196, https://doi.org/10.1029/2021EF002196, 2021.

598 An, S. I., and Wang, B.: Inter-decadal change of the structure of the ENSO mode and its impact on the

599        ENSO frequency, Journal of Climate, 13(12), 2044-2055, https://doi.org/10.1175/1520-

600        0442(2000)013<2044:ICOTSO>2.0.CO;2, 2000.

601 Bellenger, H., Guilyardi, É., Leloup, J., Lengaigne, M., and Vialard, J.: ENSO representation in climate

602        models: From CMIP3 to CMIP5, Climate Dynamics, 42(7), 1999-2018,

603        https://doi.org/10.1007/s00382-013-1783-z, 2014.

604 Birkel, S. D., Mayewski, P. A., Maasch, K. A., Kurbatov, A. V., and Lyon, B.: Evidence for a volcanic

605        underpinning of the Atlantic multidecadal oscillation, NPJ Climate and Atmospheric Science,

606        1(1), 1-7, https://doi.org/10.1038/s41612-018-0036-6, 2018.

607 Cai, W., Santoso, A., Collins, M., Dewitte, B., Karamperidou, C., Kug, J. S., ... and Zhong, W.: Changing El

608        Niño–Southern Oscillation in a warming climate. Nature Reviews Earth & Environment, 2(9),

609        628-644, https://doi.org/10.1038/s43017-021-00199-z, 2021.

610 Cai, W., Wang, G., Santoso, A., McPhaden, M. J., Wu, L., Jin, F. F., ... and Guilyardi, E.: Increased frequency

611        of extreme La Niña events under greenhouse warming, Nature Climate Change, 5(2), 132-

612        137, https://doi.org/10.1038/nclimate2492, 2015.

613 Cai, W., Borlace, S., Lengaigne, M., Van Rensch, P., Collins, M., Vecchi, G., ... and Jin, F. F.: Increasing

614        frequency of extreme El Niño events due to greenhouse warming, Nature climate

615        change, 4(2), 111-116, https://doi.org/10.1038/nclimate2100, 2014.

616 Capotondi, A., Deser, C., Phillips, A. S., Okumura, Y., & Larson, S. M.: ENSO and Pacific decadal
617     variability in the Community Earth System Model version 2, Journal of Advances in Modeling
618     Earth Systems, 12(12), e2019MS002022, https://doi.org/10.1029/2019MS002022, 2020.

619 Capotondi, A., & Sardeshmukh, P. D.: Is El Niño really changing?, Geophysical Research
620     Letters, 44(16), 8548-8556, https://doi.org/10.1002/2017GL074515, 2017.

621 Capotondi, A., Alexander, M. A., Bond, N. A., Curchitser, E. N., and Scott, J. D., Enhanced upper ocean
622     stratification with climate change in the CMIP3 models, Journal of Geophysical Research:
623     Oceans, 117(C4), https://doi.org/10.1029/2011JC007409, 2012.

624 Chen, X., and Tung, K. K.: Global-mean surface temperature variability: Space–time perspective from
625     rotated EOFs, Climate Dynamics, 51(5), 1719-1732, https://doi.org/10.1007/s00382-017-
626     3979-0, 2018.

627 Cheng, W., MacMartin, D. G., Kravitz, B., Visioni, D., Bednarz, E. M., Xu, Y., ... and Deng, X.: Changes in
628     Hadley circulation and intertropical convergence zone under strategic stratospheric aerosol
629     geoengineering, npj Climate and Atmospheric Science, 5(1), 32,
630     https://doi.org/10.1038/s41612-022-00254-6, 2022.

631 Cheng, L., Trenberth, K. E., Fasullo, J., Boyer, T., Abraham, J., and Zhu, J.: Improved estimates of ocean
632     heat content from 1960 to 2015, Science Advances, 3(3), e1601545,
633     https://doi.org/10.1126/sciadv.1601545, 2017.

634 Cook, B. I., Mankin, J. S., Marvel, K., Williams, A. P., Smerdon, J. E., and Anchukaitis, K. J.: Twenty-first
635     century drought projections in the CMIP6 forcing scenarios, Earth's Future, 8(6),
636     e2019EF001461, https://doi.org/10.1029/2019EF001461, 2020.

637 Dagon, K., and Schrag, D. P.: Exploring the effects of solar radiation management on water cycling in
638     a coupled land–atmosphere model. Journal of Climate, 29(7), 2635-2650,
639     https://doi.org/10.1175/JCLI-D-15-0472.1, 2016.

640 Danabasoglu, G., Lamarque, J. F., Bacmeister, J., Bailey, D. A., DuVivier, A. K., Edwards, J., ... and Strand,
641     W. G.: The community earth system model version 2 (CESM2), Journal of Advances in
642     Modeling Earth Systems, 12(2), e2019MS001916, https://doi.org/10.1029/2019MS001916,
643     2020.

644 Enfield, D. B., Mestas-Nuñez, A. M., and Trimble, P. J.: The Atlantic multidecadal oscillation and its
645     relation to rainfall and river flows in the continental US, Geophysical Research
646     Letters, 28(10), 2077-2080, https://doi.org/10.1029/2000GL012745, 2001.

647 Eyring, V., Bony, S., Meehl, G. A., Senior, C. A., Stevens, B., Stouffer, R. J., and Taylor, K. E.: Overview of
648     the Coupled Model Intercomparison Project Phase 6 (CMIP6) experimental design and

649      organization, Geoscientific Model Development, 9(5), 1937-1958,
650      https://doi.org/10.1029/2000GL012745, 2016.

651 Fang, C., Wu, L., and Zhang, X.: The impact of global warming on the Pacific Decadal Oscillation and
652      the possible mechanism, Advances in Atmospheric Sciences, 31(1), 118-130,
653      https://doi.org/10.1007/s00376-013-2260-7, 2014.

654 Fasullo, J. T. and Richter, J. H.: Scenario and Model Dependence of Strategic Solar Climate Intervention
655      in CESM, EGUsphere [preprint], https://doi.org/10.5194/egusphere-2022-779, 2022.

656 Fasullo, J. T., Phillips, A. S., and Deser, C.: Evaluation of leading modes of climate variability in the
657      CMIP archives, Journal of Climate, 33(13), 5527-5545, https://doi.org/10.1175/JCLI-D-19-
658      1024.1, 2020.

659 Fedorov, A. V., Hu, S., Wittenberg, A. T., Levine, A. F., and Deser, C.: ENSO Low-Frequency Modulation
660      and Mean State Interactions, El Niño Southern Oscillation in a changing climate, 173-198,
661      https://doi.org/10.1002/9781119548164.ch8, 2020.

662 Fedorov, A. V., and Philander, S. G.: A stability analysis of tropical ocean–atmosphere interactions:
663      Bridging measurements and theory for El Niño, Journal of Climate, 14(14), 3086-3101,
664      https://doi.org/10.1175/1520-0442(2001)014<3086:ASAOTO>2.0.CO;2, 2001.

665 Field, C. B., and Barros, V. R. (Eds.): Climate change 2014–Impacts, adaptation and vulnerability:
666      Regional aspects, Cambridge University Press, 2014.

667 Fredriksen, H. B., Berner, J., Subramanian, A. C., and Capotondi, A.: How does El Niño–Southern
668      Oscillation change under global warming—A first look at CMIP6, Geophysical Research
669      Letters, 47(22), e2020GL090640, https://doi.org/10.1029/2020GL090640, 2020.

670 Gabriel, C. J., and Robock, A.: Stratospheric geoengineering impacts on El Niño/Southern
671      Oscillation, Atmospheric Chemistry and Physics, 15(20), 11949-11966,
672      https://doi.org/10.5194/acp-15-11949-2015, 2015.

673 Gertler, C. G., O'Gorman, P. A., Kravitz, B., Moore, J. C., Phipps, S. J., and Watanabe, S.: Weakening of the
674      extratropical storm tracks in solar geoengineering scenarios, Geophysical Research
675      Letters, 47(11), e2020GL087348, https://doi.org/10.1029/2020GL087348, 2020.

676 Ghil, M., Allen, M. R., Dettinger, M. D., Ide, K., Kondrashov, D., Mann, M. E., ... and Yiou, P.: Advanced
677      spectral methods for climatic time series, Reviews of geophysics, 40(1), 3-1,
678      https://doi.org/10.1029/2000RG000092, 2002.

679 Greene, C. A., Thirumalai, K., Kearney, K. A., Delgado, J. M., Schwanghart, W., Wolfenbarger, N. S., ... and
680      Blankenship, D. D.: The climate data toolbox for MATLAB, Geochemistry, Geophysics,
681      Geosystems, 20(7), 3774-3781, https://doi.org/10.1029/2019GC008392, 2019.

682 Grinsted, A., Moore, J.C., and Jevrejeva, S.: Application of the cross wavelet transform and wavelet
683     coherence to geophysical time series, Nonlinear Proc. Geoph. 11 (5-6), 561-566,
684     https://doi.org/10.5194/npg-11-561-2004, 2004.

685 Haarsma, R. J., Roberts, M. J., Vidale, P. L., Senior, C. A., Bellucci, A., Bao, Q., Chang, P., Corti, S., Fučkar,
686     N. S., Guemas, V., von Hardenberg, J., Hazeleger, W., Kodama, C., Koenigk, T., Leung, L. R., Lu,
687     J., Luo, J.-J., Mao, J., Mizielinski, M. S., Mizuta, R., Nobre, P., Satoh, M., Scoccimarro, E., Semmler,
688     T., Small, J., and von Storch, J.-S.: High Resolution Model Intercomparison Project
689     (HighResMIP v1.0) for CMIP6, Geosci. Model Dev., 9, 4185–4208,
690     https://doi.org/10.5194/gmd-9-4185-2016, 2016.

691 Holmes, R. M., McGregor, S., Santoso, A., and England, M. H.: Contribution of tropical instability waves
692     to ENSO irregularity, Climate Dynamics, 52(3), 1837-1855,
693     https://doi.org/10.1007/s00382-018-4217-0, 2019.

694 Hu, Z. Z., and Wu, Z.: The intensification and shift of the annual North Atlantic Oscillation in a global
695     warming scenario simulation, Tellus A: Dynamic Meteorology and Oceanography, 56(2), 112-
696     124, https://doi.org/10.3402/tellusa.v56i2.14403, 2004.

697 Hua, W., Dai, A., and Qin, M.: Contributions of internal variability and external forcing to the recent
698     Pacific decadal variations, Geophysical Research Letters, 45(14), 7084-7092,
699     https://doi.org/10.1029/2018GL079033, 2018.

700 Intergovernmental Panel on Climate Change (IPCC): Working Group I Contribution to the Sixth
701     Assessment Report (AR6), Climate Change 2021: The Physical Science Basis, 2021. Available
702     online: https://www.ipcc.ch/assessment-report/ar6/, 2007.

703 Joyce, T. M.: One hundred plus years of wintertime climate variability in the eastern United States, J.
704     Clim., 15, 1076–1086, https://doi.org/10.1175/1520-
705     0442(2002)015<1076:OHPYOW>2.0.CO;2, 2002.

706 Knutti, R., Stocker, T. F., Joos, F., and Plattner, G. K.: Constraints on radiative forcing and future climate
707     change from observations and climate model ensembles, Nature, 416(6882), 719-723,
708     https://doi.org/10.1038/416719a, 2002.

709 Jun, M., Knutti, R., and Nychka, D. W.: Spatial analysis to quantify numerical model bias and
710     dependence: how many climate models are there?, Journal of the American Statistical
711     Association, 103(483), 934-947, https://doi.org/10.1198/016214507000001265, 2008.

712 Kravitz, B., MacMartin, D. G., Mills, M. J., Richter, J. H., Tilmes, S., Lamarque, J. F., Tribbia, J. J. and Vitt,
713     F.: First simulations of designing stratospheric sulfate aerosol geoengineering to meet

multiple simultaneous climate objectives, Journal of Geophysical Research: Atmospheres, 122, 12,616–12,634, https://doi.org/10.1002/2017JD026874, 2017.

Kravitz, B., Caldeira, K., Boucher, O., Robock, A., Rasch, P. J., Alterskjaer, K., ... and Yoon, J. H.: Climate model response from the geoengineering model intercomparison project (GeoMIP), Journal of Geophysical Research: Atmospheres, 118(15), 8320-8332, https://doi.org/10.1002/jgrd.50646, 2013.

Latif, M., and Keenlyside, N. S.: El Niño/Southern Oscillation response to global warming, Proceedings of the National Academy of Sciences, 106(49), 20578-20583, https://doi.org/10.1073/pnas.0710860105, 2009.

Mantua, N., and Hare, S.: The Pacific Decadal oscillation, J. Oceanogr. 58 (1), 35–44. http://dx.doi.org/10.1023/A:1015820616384, 2002.

Mantua, N. J., Hare, S. R., Zhang, Y., Wallace, J. M., and Francis, R. C.: A Pacific interdecadal climate oscillation with impacts on salmon production, Bulletin of the american Meteorological Society, 78(6), 1069-1080, https://doi.org/10.1175/1520-0477(1997)078<1069:APICOW>2.0.CO;2, 1997.

Masson-Delmotte, V., Zhai, P., Pirani, A., Connors, S. L., Péan, C., Berger, S., ... and Zhou, B.: Climate change 2021: the physical science basis, Contribution of working group I to the sixth assessment report of the intergovernmental panel on climate change, 2, https://10.1017/9781009157896, 2021.

Masson, S., Terray, P., Madec, G., Luo, J. J., Yamagata, T., and Takahashi, K.: Impact of intra-daily SST variability on ENSO characteristics in a coupled model, Climate dynamics, 39(3), 681-707, https://doi.org/10.1007/s00382-011-1247-2, 2012.

Mills, M. J., Richter, J. H., Tilmes, S., Kravitz, B., MacMartin, D. G., Glanville, A. A., Tribbia, J. J., Lamarque, J. F., Vitt, F., Schmidt, A. and Gettelman, A.: Radiative and chemical response to interactive stratospheric sulfate aerosols in fully coupled CESM1(WACCM), Journal of Geophysical Research: Atmospheres, 122, 13,061–13,078, https://doi.org/10.1002/2017JD027006, 2017.

Meinshausen, M., Lewis, J., McGlade, C., Gütschow, J., Nicholls, Z., Burdon, R., ... and Hackmann, B.: Realization of Paris Agreement pledges may limit warming just below 2° C, Nature, 604(7905), 304-309, https://doi.org/10.1038/s41586-022-04553-z, 2022.

Moore, J. C., Yue, C., Zhao, L., Guo, X., Watanabe, S., and Ji, D.: Greenland ice sheet response to stratospheric aerosol injection geoengineering, Earth's Future, https://doi.org/10.1029/2019EF001393, 2019.

747 Moore, J. C., Rinke, A., Yu, X., Ji, D., Cui, X., Li, Y., Alterskjaer, K., Kristjánsson, J. E., Muri, H., Boucher, O.
748     and Huneeus, N.: Arctic sea ice and atmospheric circulation under the GeoMIP G1 scenario,
749     Journal of Geophysical Research: Atmospheres, 119, 567–583,
750     https://doi.org/10.1002/2013JD021060, 2014.

751 Moron, V., Vautard, R., and Ghil, M.: Trends, interdecadal and interannual oscillations in global sea-
752     surface temperatures, Climate Dynamics, 14(7), 545-569,
753     https://doi.org/10.1007/s003820050241, 1998.

754 Riahi, K., Rao, S., Krey, V., Cho, C., Chirkov, V., Fischer, G., ... and Rafaj, P.: RCP 8.5—A scenario of
755     comparatively high greenhouse gas emissions, Climatic change, 109(1), 33-57,
756     https://doi.org/10.1007/s10584-011-0149-y, 2011.

757 Robock, A.: Volcanic eruptions and climate, *Reviews of Geophysics*, 38(2), 191–
758     219, https://doi.org/10.1029/1998RG000054, 2000.

759 Scafetta, N.: Testing the CMIP6 GCM Simulations versus surface temperature records from 1980–
760     1990 to 2011–2021: High ECS is not supported, Climate, 9(11),
761     161, https://doi.org/10.3390/cli9110161, 2021.

762 Simpkins, G.: Breaking down the NAO–AO connection, Nature Reviews Earth & Environment, 2(2),
763     88-88, https://doi.org/10.1038/s43017-021-00139-x, 2021.

764 Simpson, I. R., Bacmeister, J., Neale, R. B., Hannay, C., Gettelman, A., Garcia, R. R., ... and Richter, J. H.:
765     An evaluation of the large-scale atmospheric circulation and its variability in CESM2 and
766     other CMIP models, Journal of Geophysical Research: Atmospheres, 125(13),
767     e2020JD032835, https://doi.org/10.1029/2020JD032835, 2020.

768 Shukla, J.: Predictability in the midst of chaos: A scientific basis for climate
769     forecasting, science, 282(5389), 728-731, https://doi.org/10.1126/science.282.5389.728,
770     1998.

771 Sutton, R. T., and Hodson, D. L.: Climate response to basin-scale warming and cooling of the North
772     Atlantic Ocean, Journal of Climate, 20(5), 891–907, https://doi.org/10.1175/JCLI4038.1,
773     2007.

774 Tilmes, S., MacMartin, D. G., Lenaerts, J. T. M., van Kampenhout, L., Muntjewerf, L., Xia, L., Harrison, C.
775     S., Krumhardt, K. M., Mills, M. J., Kravitz, B., and Robock, A.: Reaching 1.5 and 2.0 °C global
776     surface temperature targets using stratospheric aerosol geoengineering, Earth Syst. Dynam.,
777     11, 579–601, https://doi.org/10.5194/esd-11-579-2020, 2020.

778 Tilmes, S., Richter, J. H., Kravitz, B., MacMartin, D. G., Mills, M. J., Simpson, I. R., Glanville, A. S., Fasullo,
779     J. T., Phillips, A. S., Lamarque, J. F. and Tribbia, J.: CESM1(WACCM) Stratospheric Aerosol

Geoengineering Large Ensemble Project, Bulletin of the American Meteorological Society, 99, 2361–2371. https://doi.org/10.1175/BAMSD-17-0267.1, 2018.

Tjiputra, J. F., Grini, A., and Lee, H.: Impact of idealized future stratospheric aerosol injection on the large-scale ocean and land carbon cycles, Journal of Geophysical Research: Biogeosciences, 121(1), 2-27, https://doi.org/10.1002/2015JG003045, 2016.

Trenberth, K. E.: The definition of El Niño, Bulletin of the American Meteorological Society, 78(12), 2771-2778, https://doi.org/10.1175/1520-0477(1997)078<2771:TDOENO>2.0.CO;2, 1997.

Tsonis, A. A., Swanson, K., and Kravtsov, S.: A new dynamical mechanism for major climate shifts, Geophysical Research Letters, 34(13), https://doi.org/10.1029/2007GL030288, 2007.

Undorf, S., Bollasina, M. A., Booth, B. B. B., and Hegerl, G. C.: Contrasting the effects of the 1850–1975 increase in sulphate aerosols from North America and Europe on the Atlantic in the CESM, Geophysical Research Letters, 45(21), 11-930, https://doi.org/10.1029/2018GL079970, 2018.

Visioni, D., MacMartin, D. G., Kravitz, B., Lee, W., Simpson, I. R., and Richter, J. H.: Reduced poleward transport due to stratospheric heating under stratospheric aerosols geoengineering, Geophysical Research Letters, 47(17), e2020GL089470, https://doi.org/10.1029/2020GL089470, 2020.

Wang, G., Swanson, K. L., and Tsonis, A. A.: The pacemaker of major climate shifts, Geophysical Research Letters, 36(7), https://doi.org/10.1029/2008GL036874, 2009.

Wang, C., and Dong, S.: Is the basin-wide warming in the North Atlantic Ocean related to atmospheric carbon dioxide and global warming?, Geophysical Research Letters, 37(8), https://doi.org/10.1029/2010GL042743, 2010.

Wang, T., Otterå, O. H., Gao, Y., and Wang, H.: The response of the North Pacific Decadal Variability to strong tropical volcanic eruptions, Climate Dynamics, 39, 2917-2936, https://doi.org/10.1007/s00382-012-1373-5, 2012.

Watson, A. J., Schuster, U., Bakker, D. C., Bates, N. R., Corbière, A., González-Dávila, M., ... and Wanninkhof, R.: Tracking the variable North Atlantic sink for atmospheric $CO_2$. Science, 326(5958), 1391-1393, https://doi.org/10.1126/science.1177394, 2009.

Westervelt, D. M., Conley, A. J., Fiore, A. M., Lamarque, J.-F., Shindell, D. T., Previdi, M., Mascioli, N. R., Faluvegi, G., Correa, G., and Horowitz, L. W.: Connecting regional aerosol emissions reductions to local and remote precipitation responses, Atmospheric Chemistry and Physics Discussions, 18, 12,461–12,475. https://doi.org/10.5194/acp-2018-516, 2018.

813 Xie, M., Moore, J. C., Zhao, L., Wolovick, M., and Muri, H.: Impacts of three types of solar geoengineering
814      on the Atlantic Meridional Overturning Circulation, Atmospheric Chemistry and
815      Physics, 22(7), 4581-4597, https://doi.org/10.5194/acp-22-4581-2022, 2022.

816 Yue, C., Schmidt, L. S., Zhao, L., Wolovick, M., and Moore, J. C.: Vatnajökull mass loss under solar
817      geoengineering due to the North Atlantic meridional overturning circulation, Earth's
818      Future, 9(9), e2021EF002052, https://doi.org/10.1029/2021EF002052, 2021.

819 Yun, K. S., Lee, J. Y., Timmermann, A., Stein, K., Stuecker, M. F., Fyfe, J. C., and Chung, E. S.: Increasing
820      ENSO–rainfall variability due to changes in future tropical temperature–rainfall
821      relationship, Communications Earth & Environment, 2(1), 1-7,
822      https://doi.org/10.1038/s43247-021-00108-8, 2021.

823 Zhang, L., and Delworth, T. L.: Simulated response of the Pacific decadal oscillation to climate
824      change, Journal of Climate, 29(16), 5999-6018, https://doi.org/10.1175/JCLI-D-15-0690.1,
825      2016.

826 Zhang, R., and Delworth, T. L.: Impact of Atlantic multidecadal oscillations on India/Sahel rainfall and
827      Atlantic hurricanes, Geophysical research letters, 33(17),
828      https://doi.org/10.1029/2006GL026267, 2006.